Program Digest, 2019 IEEE International Ultrasonics Symposium (IUS)
Glasgow, Scotland, October 6-9, 2019

Advancing the Feasible Microbubble Concentration in Super-Resolution

Marion Piepenbrock, Anna Brieden, Stefanie Dencks, and Georg Schmitz
Ruhr University Bochum
Chair for Medical Engineering
Bochum, Germany
(marion.piepenbrock; anna.brieden@rub.de; stefanie.dencks; georg.schmitz)@ruhr-uni-bochum.de

***Abstract*—For the reconstruction of the microvasculature from contrast-enhanced ultrasound sequences with ultrasound localization microscopy, it is neccessary that a vessel is flown through by at least one microbubble (MB). Therefore, the reconstruction degree can be increased by either long acquisition times or by using high MB concentrations. However, in clinical applications the measurement times are usually limited. Thus, an adequate method for the detection of the MB is essential that ensures an accurate localization of single MB even in case of overlaying point-spread functions (PSFs) when using high MB concentrations. Therefore, we investigated the performance of sparsity based ultrasound hemodynamic super-resolution (SUSHI), and also expanded it to depth dependent PSFs. We applied the method to varying MB concentrations, analyzed different implementations of SUSHI and compared it to standard detection methods (Gauss detection and the centroid detection). The sparsity driven super-resolution with depth dependent PSFs showed the highest sensitivity for high MB concentrations. The Gauss detection yielded the lowest error rates. The centroid detection failed with increasing MB concentration.**

***Index Terms*—Localization, microbubble detection, point-spread function, sparsity driven super-resolution, ultrasound localization microscopy**

I. Introduction

Ultrasound localization microscopy ()ULM) relies on the subwavelength localization of individual MB to reconstruct the microvasculature. Recently, we have shown that also in clinical measurements detailed information on the morphology and perfusion of vessels can be obtained [1][2]. However, a high enough number of microbubbles (MBs) has to be detected to get a good mapping of the vasculature [3]. In clinical applications, higher MB concentrations are preferred to long acquisitions times. Since high MB concentrations lead to overlapping PSFs, the accurate localization of individual MB is limited, and an adequate detection method is essential. Recently, van Sloun et al. presented the implementation of the sparsity based ultrasound super-resolution hemodynamic imaging (SUSHI) to CEUS frames to detect individual MBs, even in case of small distances [4]. We implemented this algorithm and additionally used depth dependent PSFs instead of an ideal Gauss kernel. The algorithm was applied to B-mode data as well as to RF data. The detection sensitivity and the localization accuracy was evaluated depending on the MB concentration, or rather on the expected minimal distance of MBs. The results were also compared to the standard detection methods (convolution with a Gaussian kernel followed by a local maxima detection and centroid detection).

This work was supported by the DFG under the Grants SCHM1171/4-1 and KI1072/11-1.

II. Material and Methods

A. Sparsity Driven Super-Resolution

Sparsity driven super resolution is a method used in the fluorescence photo-activated localization microscopy (fPALM) to get high resolved images of the vasculature [5]. In [6], the method was applied to CEUS data for the first time, called sparsity-based ultrasound super-resolution hemodynamic imaging (SUSHI), and van Sloun et al. presented a frame-to-frame implementation of SUSHI to detect single MBs in CEUS data [4]. The method is based on the knowledge about the PSF of a single MB in CEUS data. Additionally, a sparse image of MBs is assumed. This leads to the minimization problem

$$||f_{in} - Af_{out}||_2^2 + \lambda||f_{out}||_0 \qquad f_{out} \geq 0, \tag{1}$$

where f_{in} is the vectorized input image and f_{out} the vectorized output image. The output image is a sparse, super-resolved MB image which ideally is a binary matrix. The matrix A is built with vectorized PSFs for each image pixel. The product of A and the sparse image f_{out} corresponds to a convolution. Because the output is required to be sparse, the L_0-norm is used for regularization. The parameter λ is a weighting factor for the regularization. Since the L_0-norm is not solvable, the L_1-norm is used instead

$$||f_{in} - Af_{out}||_2^2 + \lambda||f_{out}||_1 \qquad f_{out} \geq 0. \tag{2}$$

This minimization problem is solved using the fast iterative shrinkage thresholding algorithm (FISTA) [7], modified to only compute positive values for f_{out}.

In [4], the fit of a rotated anisotropic 2D Gauss kernel was used as PSF to compute the matrix A. We instead simulated depth dependent PSFs with Field II [8] in Matlab to improve the localization. The simulations were computed with the settings described in section II-D.

For computational efficiency, the CEUS images were subdivided into blocks which were evaluated separately. The interpolated grid for MB detection had a resolution of 10 μm in axial and lateral direction.

B. Centroid Detection

For the centroid detection, a thresholding is carried out first, and single bright points considered to be noise, are deleted. Afterwards, it is searched for regions of higher intensity which are assumed to belong to MBs. The centroids of these regions are defined to be the MB positions [10], [11].

C. Gauss Detection

For the Gauss detection, the MB image is convolved with a Gaussian-kernel matching the size of the ultrasound systems' PSF. Afterwards, a thresholding is carried out and the image is interpolated to finally detect the local maxima on a super-resolved grid [12].

D. Simulations

To evaluate the performance of the algorithm regarding the minimum distances between the MB, Field II [8] simulations were carried out. The MBs were assumed to be point scatterers and uniformly distributed in lateral and axial direction in a phantom. The phantom width was set to7 mm and the height to 15 mm. The settings were chosen according to a clinical application [2] and resemble typical settings of the 10 MHz PLT 1005BT linear transducer of the Aplio 500 (Canon Medical Systems, Otawara, Japan). In the simulations, two foci in axial direction were realized, whose regions were combined to get the complete image. The point-spread-function is characterized by a full width half maximum of 560 µm axially and 780 µm laterally [1].

For the localization of individual MBs, a distance of less than the half width half maximum (HWHM) between two MBs is assumed to be critical for separation. Therefore, these distances are of interest for the analysis of the MB detection in case of high MB concentrations. The minimal expected distance d between MBs was evaluated assuming that the probability of detecting MBs is Poisson distributed. The probability distribution function $F_X(x(k>0))$ describes the probability to detect k MBs within a radius x, and is based on the Poisson distributed probability of detecting no MBs $(P(X(k=0)))$:

$$F_X(x(k>0)) = 1 - P(X(k=0)) = 1 - e^{-C\pi x^2}. \quad (3)$$

Hence, the probability density function $f_X(x(k>0))$ results in

$$f_X(x(k>0)) = 2C\pi x e^{-C\pi x^2}. \quad (4)$$

The minimum expected distance d is defined as the expected value of X:

$$d = E(X) = \int_0^\infty x \cdot f_X(x)\,\mathrm{d}x = \frac{1}{2\cdot\sqrt{C}}. \quad (5)$$

MB concentrations from 3 to 80$\cdot 10^5$ MBm^{-2} were simulated leading to the expected minimal distances of 912.9 µm to 176.8 µm. The relationship is shown in Fig. 1. The critical regions in which d is lower the HWHM in lateral and in axial direction are coloured in yellow and red, respectively.

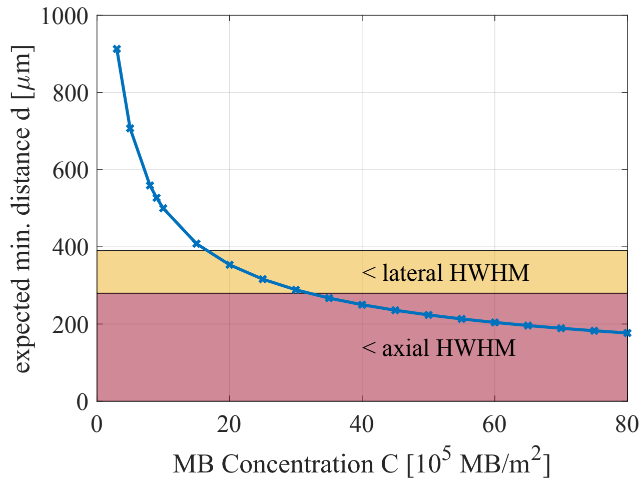

Fig. 1: Expected minimal distance of MB as a function of the MB concentration. The distances smaller than the HWHM in lateral (yellow) and in axial (red) direction are coloured.

In these simulations, a successful separation of the foreground (MB) from the background (tissue) without artefacts was assumed to enable the performance analysis of the MB detection depending on the MB concentration without other influencing factors.

E. Quality Criteria

The performance of the MB detection was evaluated by the sensitivity Se and the error rate ER:

$$\mathrm{Se} = \frac{N_{\mathrm{TP}}}{N_{\mathrm{GT}}} \qquad \mathrm{ER} = \frac{N_{\mathrm{FP}}}{N_{\mathrm{FP}} + N_{\mathrm{TP}}}. \quad (6)$$

N_{TP} is the number of true positive detections, N_{GT} the ground truth number of detections, N_{FP} the number of false positive detections. An MB was assigned to a simulated MB if its position was detected within the standard deviation of the PSF to the ground truth position.

Furthermore, the accuracy of MB localization was evaluated by the distance between ground truth and detected position. The lateral and axial deviations were assessed separately, as well as the Euclidean distance for both. The mean values and standard deviations were calculated as a function of the MB concentration.

III. Results

A. Comparison of different SUSHI Implementations

The sensitivity and error rate for the different implementations of SUSHI are shown in Fig. 2. The sensitivity for both SUSHI algorithms applied to B-Mode data, using one ideal Gauss kernel as PSF (red) and the depth dependent PSFs (dark red), is comparable. For large expected minimum distances, the sensitivity is 1 and decreases with decreasing distance as to be expected. For distances larger than the lateral HWHM, the sensitivity is always higher than 80%. For an expected minimal distance of 176 µm, the sensitivity decreases to 45%. Regarding the error rate, these two implementations show slight differences. For expected minimum distances between 500 µm to 900 µm, the error rate is between 10% and 25% for SUSHI with the ideal Gauss kernel and between 8% to 15% using depth dependent PSFs.

The implementation with depth dependent PSFs applied to RF data shows a similar behaviour of the sensitivity for distances larger than the lateral HWHM. With further decreasing distances, the sensitivity remains higher than for the other two implementations. For a distance of 176 µm, the sensitivity is around 15% higher compared to the detection on B-mode data. Since the error rate is in a similar range as when using the ideal Gauss kernel on B-mode data, this is a clear improvement. Compared to using the depth dependent PSFs on B-mode data, the advantage of the higher sensitivity disappears because also the error rate is approximately 10% higher.

In Fig. 3, the localization error of the MB detection is shown separately for the lateral (a) and axial direction (b), as well as for the Euclidean distance considering both directions (c). For all SUSHI implementations, the positions are localized more precise in axial than in lateral direction, but with the same accuracy. The standard deviations of the localization error in lateral direction increase with decreasing distance and are between 10 µm to 100 µm. No substantial differences for the three different implementations are observable. Regarding the localization error in axial direction, using depth dependent PSFs on RF data leads to more precise results (standard deviations between 10 µm to 25 µm) than the other two implementations (standard deviations between 20 µm to 50 µm).

Calculating the Euclidean distance leads to a bias of 20 µm to 100 µm, dependent on the distance. Using the implementation on RF data leads to a slightly lower bias. However, for all implementations the accuracy and the precision gets worse for high MB concentrations.

B. Comparison of Detection Methods

Fig. 4 illustrates the performance of the investigated detection methods: the Gauss detection (blue), centroid detection (green) and SUSHI (dark red). Because the Gauss detection and centroid detection are both applied to B-mode data, these are compared to the SUSHI implementation with depth dependent PSFs applied to B-mode data.

The sensitivity of the Gauss detection decreases from 92% for the largest distance to 21% for the shortest distance. For distances larger than 500 µm, the sensitivity is higher than 80%. For shorter distances, it decreases to 65% at the lateral HWHM. For the lowest distance of 176 µm, the sensitivity drops down to 21%. However, the Gauss detection has the lowest error rate which is only slightly influenced by the distance between the MBs.

The centroid detection already starts with a low sensitivity of 74% for the largest distance, and quickly decreases to 0 for the lowest distance.

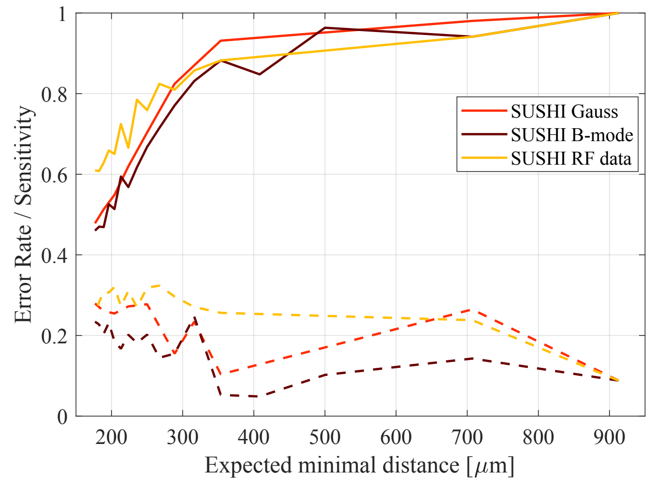

Fig. 2: Sensitivity and error rate of applying SUSHI to the simulations: one ideal Gauss kernel applied to B-mode data (red), depth dependent PSFs applied to B-mode data (dark red) and depth dependent PSFs applied to RF data (orange). Solid lines: sensitivity; dashed lines: error rate.

As described before, the SUSHI algorithm leads to a sensitivity of 1 for the largest distance and is over 80% for distances larger than the lateral HWHM. This means an improvement of around 20% compared to the Gauss detection. For the lowest distance, it yields a sensitivity of 41% which is again an improvement of 20%. However, with an error rate of 10% to 20%, it exceeds the error rate of the Gauss detection.

IV. Discussion and Outlook

The analysis has shown that the centroid detection is only suitable for low MB concentrations because it cannot handle overlapping PSFs. Close MBs are interpreted as one large bolus. Hence, the MB position is detected at the centroid of multiple MBs which does not correspond to one of the true MB positions. Thus, the sensitivity is low, and the error rate increases with the concentration.

In contrast, the Gauss detection performs well and is characterized by a low error rate. However, the sensitivity is low for high MB concentrations.

SUSHI is well applicable to also high MB concentrations, independent of the implementation. However, using depth dependent PSFs, especially on RF data, improves the sensitivity compared to using one ideal Gauss kernel on B-mode data. The fact that the sensitivity is higher, but the error rate is lower using the depth dependent PSFs on RF data instead of on B-mode data, signifies that this could be effected by the choice of the weighting factor λ. In contrast, the implementations on B-mode data for low distances indicate that using depth dependent PSFs is an improvement to using one ideal Gauss kernel. The sensitivity is similar for both, but the error rate is higher for the implementation with the ideal Gauss kernel.

The parameter λ weights the regularization and can influence the detection results. A high value for λ leads to a sparse image which means a low number of detections, thus a low

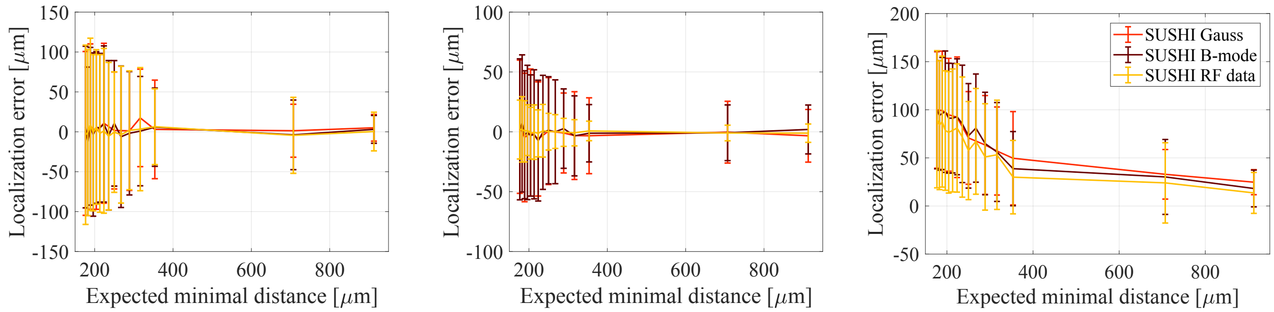

(a) lateral error (b) axial error (c) euclidean norm

Fig. 3: Localization error of detected MBs (distance between ground truth and detected positions, in lateral (a) and the axial direction (b), as well as the Euclidean norm (c), for different implementations of SUSHI: one ideal Gauss kernel applied to B-mode (red), depth dependent PSFs applied to B-mode data (brown) and depth dependent PSFs applied to RF data (orange).

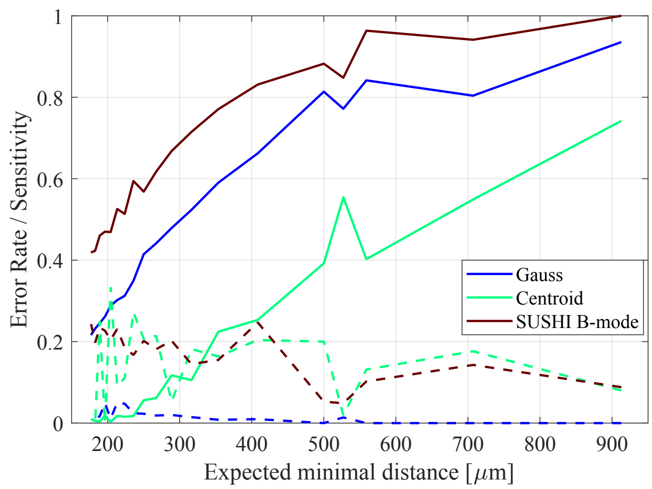

Fig. 4: Sensitivity and error rate when applying the Gauss detection (blue), the centroid detection (green) and SUSHI (dark red) with depth dependent PSFs applied to B-mode data. Solid line: sensitivity; dashed line: error rate.

error rate, but also a low sensitivity. In contrast, it is vice versa for a low λ. It has to be adapted for RF data and B-mode data and maybe, it should also be varied dependent on the MB concentration. Probably, approaches based on deep learning [9] should be preferred to get a higher computational efficiency and to eliminate the uncertainty because of λ.

Concluding, these methods are applicable to high MB concentrations and the depth dependent, simulated PSFs should be preferred to the ideal Gauss kernel. MB concentrations can be increased to get a faster reconstruction of the microvasculature, but also dense vascularized organs that lead to close MBs in neighbouring vessels, can be processed. However, localizations with distances lower than the axial HWHM of the systems PSF should be treated with caution because the localization error increases with decreasing distance. The same was observed for the localization with Gauss detection, not shown here. As further investigations, the performance tests should be carried out on noisy MB images with artefacts of the foreground-background separation.

REFERENCES

[1] T. Opacic, S. Dencks et al., ‘Motion model ultrasound localization microscopy for preclinical and clinical multiparametric tumor characterization,“ Nat. Comm., vol. 9, article number 1527, 2018.

[2] S. Dencks et al, “Clinical Pilot Application of Super-resolution US Imaging in Breast Cancer,“ IEEE Trans. Ultrason. Ferroelectr. Freq. Control, DOI: 10.1109/TUFFC.2018.2872067, 2018.

[3] S. Dencks, M. Piepenbrock, G. Schmitz, T. Opacic and F. Kiessling, “Determination of adequate measurement times for super-resolution characterization of tumor vascularization,“ Proc. IEEE International Ultrasonics Symposium (IUS), 2017.

[4] R.J.G. van Sloun, Y. C. Eldar, H. Wijkstra and M. Mischi “Sparsity-driven super-resolution in clinical contrast-enhanced ultrasound,“ Proc. IEEE International Ultrasonics Symposium (IUS), 2016.

[5] T. Dertinger, R. Colyer, G. Iyer, S. Weiss and J. Enderlein, “Fast, background-free, 3D super-resolution optical fluctuation imaging (SOFI),“ PNAS, vol. 106, no. 52, pp. 22287-22292, 2009.

[6] A. Bar-Zion, O. Solomon, C. Tremblay-Darveau, D. Adam, Y. C. Eldar, “Sparsity-based ultrasound super-resolution imaging,“ Proceeding of the 23rd European symposium on Ultrasound Contrast Imaging, pp. 156-157, ICUS, 2017.

[7] A. Beck and M. Teboulle, “A fast iterative shrinkage-thresholding algorithm for linear inverse problems.,“SIAM journal on imaging science, vol. 2, no. 1, pp. 183-202, 2009.

[8] J.A. Jensen, ‘ Field: A Program for Simulating Ultrasound Systems,“ Medical & Biological Engineering & Computing, vol. 34, pp. 351-353, 1996.

[9] R.J.G. van Sloun, O. Solomon, M. Bruce, Z. Z. Khaing, Y. C. Eldar, and M. Mischi “Deep Learning for Super-resolution Vascular Ultrasound Imaging,“ IEEE International Conference on Acoustics (ICASSP), Speech and Signal Processing, pp. 1055-1059, 2019.

[10] O. M. Viessmann, R. J. Eckersley, K. Christensen-Jeffries, M. X. Tang and C. Dunsby “Acoustic super-resolution with ultrasound and microbubbles,“ Phys. Med. Biol., vol 52, pp. 6447-6458, 2013.

[11] M. Siepman, G. Schmitz, J. Bzyl, M. Palmowski and F. Kiessling “Imaging Tumor Vascularity by Tracing Single Microbubbles,“ Proc. IEEE International Ultrasonics Symposium (IUS), 2011.

[12] D. Ackermann, G. Schmitz, “Detection and Tracking of Multiple Microbubbles in Ultrasound B-Mode Images,“ IEEE TUFFC, no 1, pp. 72-82, 2016.